J Mol Model (2015) 21:48
DOI 10.1007/s00894-015-2596-2

ORIGINAL PAPER

Electronic and optical properties of N-doped Bi_2O_3 polymorphs for visible light-induced photocatalysis

Fang Wang · Kun Cao · Yi Wu · Greta R. Patzke · Ying Zhou

Received: 25 August 2014 / Accepted: 26 January 2015

Abstract The effect of N doping on the crystal structure, electronic, and optical properties of α-Bi_2O_3 and β-Bi_2O_3 has been studied in detail based with first principle calculations. The crystallographic features of Bi_2O_3 polymorphs are not substantially changed through N doping, whereas charge transfer from Bi to N results in large variations of charge density distribution. N-doped β-Bi_2O_3 exhibits improved thermal stability due to stronger Bi-N covalent bonds and lower defect formation energy, and the convenient preparative access agrees well with experimental observations. Calculated band structures and optical properties indicate that N doping does not induce major band gap narrowing, but leads to the presence of isolated bands above the VBM induced by N 2p for both α-Bi_2O_3 and β-Bi_2O_3 which induce large red-shifts of their visible light absoprtion properties. These isolated bands act as acceptor levels and facilitate electron transition under visible light illumination through introduction of steps between VB and CB, thereby rendering the materials quite promising for photocatalytic applications.

Keywords First-principle calculations · N-doped Bi_2O_3 · Photocatalytsts

F. Wang · Y. Zhou (✉)
State Key Laboratory of Oil and Gas Reservoir Geology and Exploitation, Southwest Petroleum University, Chengdu 610500, China
e-mail: yzhou@swpu.edu.cn

F. Wang · K. Cao · Y. Wu · Y. Zhou
The Center of New Energy Materials and Technology, School of Materials Science and Engineering, Southwest Petroleum University, Chengdu 610500, China

G. R. Patzke
Department of Chemistry, University of Zurich, 8057 Zurich, Switzerland

Introduction

Although TiO_2 has been widely investigated as an outstanding photocatalytic material, it can only be activated under ultraviolet light irradiation due to its large band gap (3.2 eV for anatase and 3.0 eV for rutile), and the quick recombination of photoinduced electron–hole pairs is another limiting factor for its photochemical application [1, 2]. This triggered a worldwide search for efficient visible light-driven photocatalysts for better use of solar light resources. Among the multitude of investigated target compounds, Bi_2O_3 has attracted notable interest due to its various modifications with unique crystal structures and band gaps in the desired range [3–5]. Bi_2O_3 mainly has four polymorphs, including the monoclinic α, tetragonal β, body centered cubic γ, and face centered δ forms. Among these phases, narrow band gaps of 2.8 and 2.48 eV for α-Bi_2O_3 and β-Bi_2O_3, respectively, have been reported in most experimental studies and β-Bi_2O_3 was shown to exhibit better photocatalytic activity under visible light illumination [6, 7]. However, two major issues remain in the way of their use as effective visible light driven photocatalysts. First, the band gaps are still too wide for overall visible light absorption which would truly set the photocatalytic performance of both Bi_2O_3 modifications apart from other oxide catalysts. Second, Bi_2O_3 polymorphs are sensitive toward temperature-dependent phase transformations; e.g., the metastable high-temperature β-Bi_2O modification tends to transform into low-temperature α-Bi_2O_3 at a definite temperature [8] which would restrict the parameter window for photocatalytic applications. Doping has been proposed as an effective solution to these issues [9, 10]. A notable study on this topic demonstrated that N dopants to Bi_2O_3 induced red-shift of the visible light absorption, resulting in a significantly improved photodegradation performance [11, 12]. Moreover, nitrogen doping obviously facilitated the formation of the β-Bi_2O_3 phase. In contrast, theoretical studies on hydrogen

Published online: 19 February 2015

generation with series of co-doped β-Bi_2O_3 solid solutions showed that N doping may limit the photocatalytic applications because the doping levels could act as electron–hole recombination centers [13].

As for photocatalyst optimization via N-doping, the most widely studied target of experimental studies and theoretical simulations is still N-doped TiO_2. However, the interpretation of the influence of N-doping on the absorption behavior of TiO_2 remains somewhat controversial. Asahi et al. [14] concluded that N/O substitution in anatase TiO_2 narrowed the band gap by mixing of N2p with O2p states, leading to an extension of the absorption band edge into the visible light region. In contrast, other studies indicated that the introduction of localized gap states by N2p orbitals played a more important role in the visible light absorption process than the more obvious effect of band gap narrowing [15, 16]. Additional works pointed out that the observed absorption red shift was caused by oxygen vacancies [17]. This variety of models applied to N-doped TiO_2 inspired us to conduct new studies into the working mechanism of enhanced visible absorption for the N-doped Bi_2O_3 polymorphs as a new versatile target system.

To our knowledge, the thermal stability of N-doped α-Bi_2O_3 and β-Bi_2O_3 and the reasons for their enhanced visible light driven photocatalytic performance remain unknown to date and therefore merit detailed studies. Consequently, the present work aims for a fundamental insight into the effects of N doping on the electronic and optical properties of α-Bi_2O_3 and β-Bi_2O_3 in order to correlate the results with their expected photocatalytic properties. Such theoretical studies are fruitful for targeted experimental work on the challenging goal of improved photocatalytic performance of Bi_2O_3 via tailored N doping strategies

Computational methods

First-principle calculations were performed at the generalized gradient approximation (GGA) functional of Perdew-Wang (PW91) level [18] with the Vanderbilt-type ultrasoft pseudopotential [19] and a plane-wave expansion of the wave functions implemented in the CASTEP package [20]. The valence atom configurations are $6s^26p^3$ for Bi, $2s^22p^4$ for O, and $2s^2p^3$ for N. The structures were relaxed by using the Broyden, Fletcher, Goldfarb, and Shannon (BFGS) method [21], with cutoff energy for the plane wave basis set of 380 eV. Brillouin zone sampling was performed by using the Monkhorst-Pack grid of 2×2×2*k*-points. In the geometry relaxation, the total energy of system was converged to less than 2×10^{-6} eV/atom, the residual force to less than 0.01 eV/Å, and the displacement of atoms and residual bulk stress to less than 0.002 Å and 0.1 GPa, respectively. These parameters were determined to ensure well-converged total energies and geometry optimization calculations. The electronic structures were calculated based on the fully relaxed lattice parameters and ionic positions. Band structures were simulated along the paths connecting the high-symmetry points: Γ(0,0,0), F(0,0.5, 0), Q(0,0.5,0), and Z(0,0,0.5) in the Brillouin zone. For the calculation of the density of states (DOS), a larger 4×2×3*k*-point set was used. It is well known that the GGA method leads to an underestimation of band gaps. We therefore applied the scissor correction method [22, 23] to scale the band gaps to experimental values (2.8 eV for α-Bi_2O_3 and 2.48 eV for β-Bi_2O_3). Scissor operators were also used in calculating the optical spectra to fit the experimental value. For the N-doped crystals, studies have shown that GGA can generate reliable electronic structures of doping levels in comparison with DFT+U or DFT hybrid methods [24–26] so that this method was selected for the following study.

α-Bi_2O_3 and β-Bi_2O_3 display monoclinic and tetragonal lattice symmetry respectively, [27], both containing eight Bi atoms and 12 O atoms per unit cell. As there are two non-equivalent oxygen atoms with one bridged with two Bi atoms and another with three Bi atoms, two possible O defect positions of substitutional nitrogen were considered for constructing N-doped Bi_2O_3 polymorphs, so that four N-doped polymorphs were fully relaxed in the first place. Calculation results show that the difference of total energies on different doping sites is 0.1 eV, and the stable configurations with lower energies were considered in the following calculation as displayed in Fig. 1.

Results and discussion

Crystal structure and thermodynamic stability

The calculated lattice constants of Bi_2O_3 polymorphs and N-doped Bi_2O_3 together with their measured values are listed in Table 1. The optimized lattice constants correspond well with the measured lattice constants of α-Bi_2O_3 and β-Bi_2O_3, thereby confirming our reasonable selection of computational parameters. Comparison of the values for pure and N-doped Bi_2O_3 shows that the lattice constants do not undergo major changes upon N doping, i.e., it does not induce substantial distortions of the crystal lattice. The Bi-N bond lengths in N-doped Bi_2O_3 are generally larger than the Bi-O values for the pristine oxides (Fig. 1) due to the slightly larger ionic radius of N^{3-} compared to O^{2-}. For example, the Bi1-O1 bond in pure α-Bi_2O_3 (2.21 Å) is elongated to a Bi1-N1 bond length of 2.35 Å after doping. In short, substitution N for O induces only small changes of lattice parameters and local structure environments.

To investigate the influence of doping on the chemical bonding scenario, we compare the two-dimensional electron densities of pure and N-doped Bi_2O_3 in Fig. 2. Selected

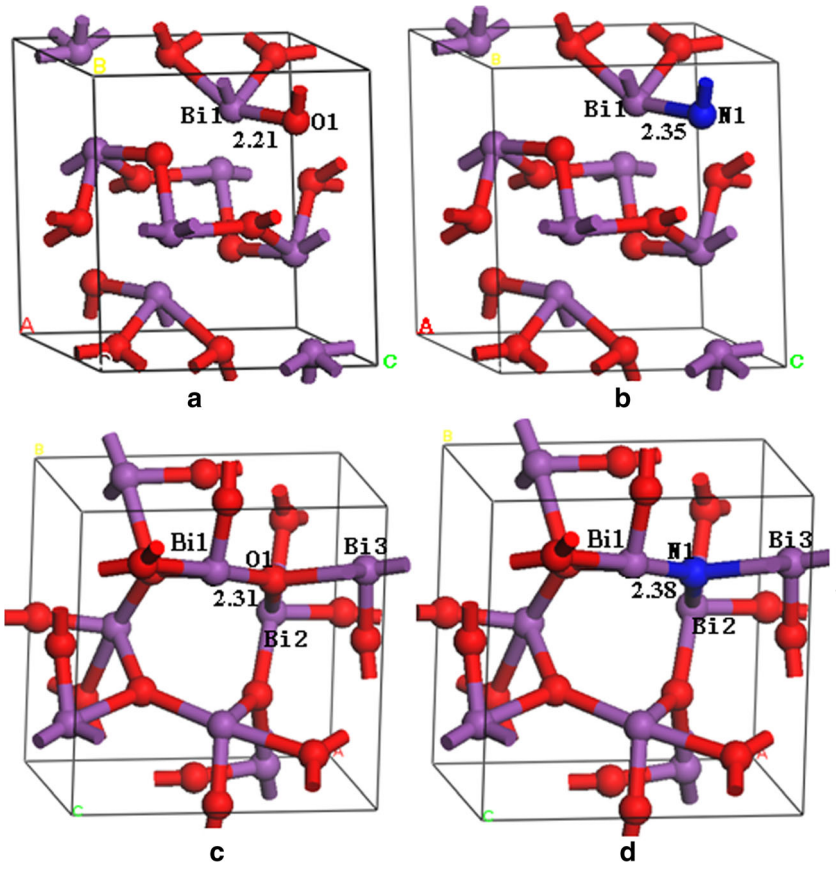

Fig. 1 Bulk structures of α-Bi_2O_3 (**a**), N-doped α-Bi_2O_3 (**b**), β-Bi_2O_3 (**c**), and N-doped β-Bi_2O_3 (**d**). *Red* oxygen; *Purple* bismuth

density regions near the doping site were displayed for the sake of clarity. The electron density around Bi and O atoms adjacent to N changes to some extent in comparison with the pure Bi_2O_3 polymorphs. N-doped β-Bi_2O_3 in particular displays more intense electron clouds around N than observed for O in pure β-Bi_2O_3, suggesting that N/O substitution leads to electron deprivation at the Bi centers, which results in changes of original charge density distribution. Such changes of charge density distribution have also been reported for Bi/N-codoped anatase TiO_2 [28]. The N dopants bind to the Bi atoms in α-Bi_2O_3 and β-Bi_2O_3, thereby increasing the covalent character of both polymorphs. To gain further insights into the charge transfer induced by N doping, electron density differences of the doped modifications are mapped in Figs. 2c and f. Obviously, electron density is accumulated around N and depleted around Bi, resulting in a charge transfer from Bi to N. Moreover, the higher charge density of N spreads out over a larger range than that of the adjacent O atom, revealing that N doping gives rise to apparent charge transfer and induces significant charge density variations in the Bi and O atoms. The charge transfer can be further analyzed by examining the Mulliken charge and overlap population as listed in Table 2. Although the absolute magnitudes of Mulliken populations have little physical meaning, the relative values can be used as an

Table 1 Relaxed lattice constants (lengths in Å and angles in °) for pure and N-doped Bi_2O_3 together with experimental values

Lattice parameter	Crystal phase			
	α-Bi_2O_3	β-Bi_2O_3	N-doped α-Bi_2O_3	N-doped β-Bi_2O_3
a	5.852 (5.849)	7.721 (7.738)	5.830	7.673
b	8.206 (8.167)	7.723 (7.738)	8.160	7.672
c	7.234 (7.509)	6.166 (5.731)	7.368	6.186
α	90.01 (90.00)	89.98 (90.00)	89.50	89.77
β	112.40 (113.00)	90.10 (90.00)	111.80	90.11
γ	90.00 (90.00)	90.02 (90.00)	90.48	90.56

[a] Data in parentheses are experimental values from ref. [27]

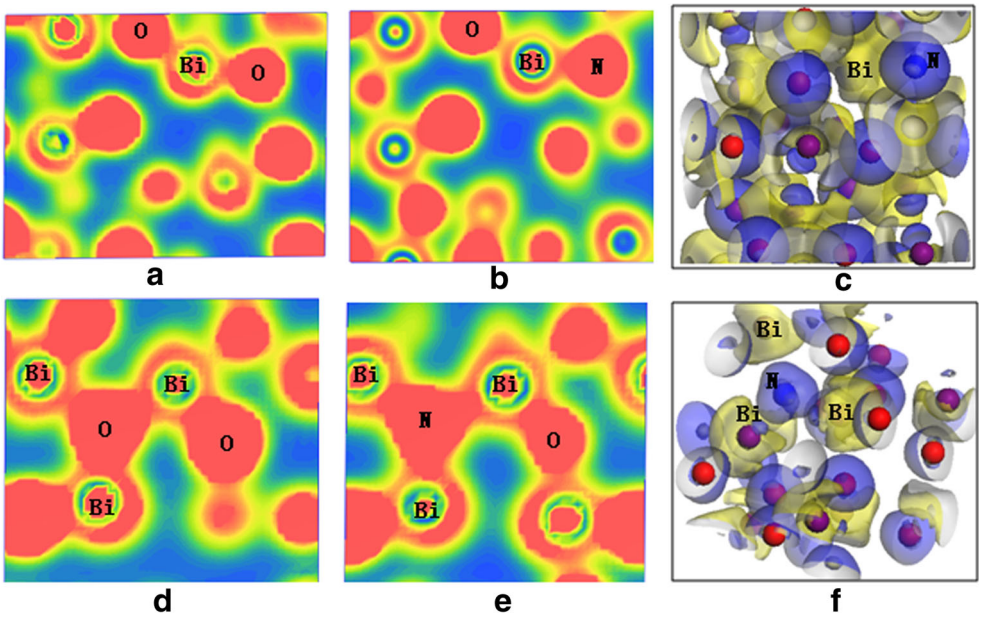

Fig. 2 Total charge densities of α-Bi_2O_3 (**a**), N-doped α-Bi_2O_3 (**b**), β-Bi_2O_3 (**d**), N-doped β-Bi_2O_3 (**e**), and electron density difference of N-doped α-Bi_2O_3 (**c**) and N-doped β-Bi_2O_3 (**f**)

indication of bond order. A higher value of the bond order shows stronger bond strength. For α-Bi_2O_3 and β-Bi_2O_3, the charge of Bi is reduced by about 0.05 e in comparison with pure Bi_2O_3, indicating charge transfer induced by N doping. This is furthermore evident from the more negative values of the electron population of N (about −0.98 e) compared to O (about −0.94 e) in pure α-Bi_2O_3 and β-Bi_2O_3, which is in line with the above electron density difference analysis. As N has one valence electron less than O, it rather acts as an electron acceptor when bonding to the adjacent Bi atoms. The bond order of Bi–N (0.15) is similar to that of Bi–O in pure α-Bi_2O_3, whereas it is considerably higher for N-doped β-Bi_2O_3 (0.34) than that in the pristine form (0.22). This could result in a better stability for N-doped β-Bi_2O_3 compared to N-doped α-Bi_2O_3. This can be supported by the defect formation energies of N-doped Bi_2O_3 polymorphs.

To compare the thermodynamic stability of N-doped Bi_2O_3 modifications, we calculated their respective defect formation energies (E_f), i.e., the energy required to introduce a N dopant into the oxide lattice, according to the following equation:

$$E_f = E_{doped} + \mu_O - \mu_N - E_{pure}, \quad (1)$$

where E_{doped} and E_{pure} are the total energies of the Bi_2O_3 polymorphs with and without N doping. μ_O and μ_N represent the chemical potential of N and O atoms which are determined by a half energy of triplet ground state O_2 and single ground state of N_2, respectively. Lower E_f values indicate favorable doping properties of the host lattice. Calculated E_f values for N-doped α-Bi_2O_3 and β-Bi_2O_3 are 4.64 and 4.50 eV, respectively, and these values are below those for N/O substitution in anatase TiO_2 ($E_f \geq 5.5$ eV) [29] and Bi_2WO_6 ($E_f \geq 5.2$ eV) [23] hosts. The results of our calculations thus show that N-doped β-Bi_2O_3 can be obtained more easily than N-doped α-Bi_2O_3, which suggests that N/O substitution in α-Bi_2O_3 leads to N-doped β-Bi_2O_3 as a more stable form, which is in agreement with the experimental observations [11].

Table 2 Mulliken populations of selected atoms and bonds for pure and N-doped Bi_2O_3

Polymorph	Element	Pure charge /e	Doped	Bond	Pure bond order	Doped
α- Bi_2O_3	Bi1	1.35	1.30	N1-Bi1	0.15	0.15
	O1	−0.93				
	N1		−0.99			
β- Bi_2O_3	Bi1	1.41	1.35	N1-Bi1	0.22	0.34
	O1	−0.95				
	N1		−0.98			

Band structures and density of states

Contemporary photocatalyst design depends to a large extent on precise insight into the correlation between electronic structure and semiconducting properties [22, 23, 25]. Consequently, the influence of N doping on the electronic structures, band structures, and corresponding density of states (DOS) is illustrated for both host modifications in Figs. 3 and 4. The main features are summarized as follows: (i) α-Bi_2O_3 and β-Bi_2O_3 display indirect and direct band gaps, respectively, with calculated band gaps of 2.8 and 2.46 eV which are in accord with experimental values 2.8 and 2.48 eV [7]. The smaller

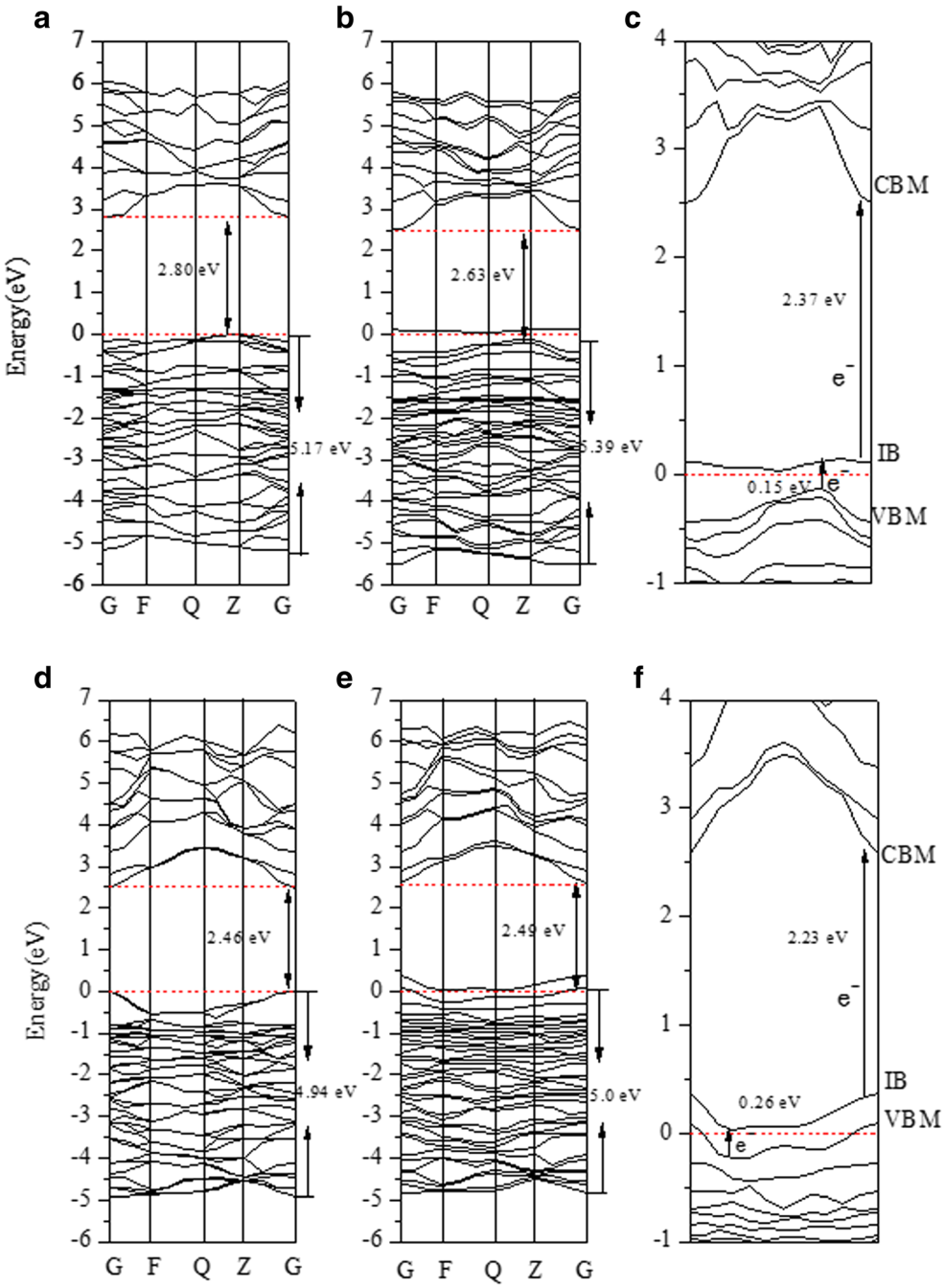

Fig. 3 Band structures of pure α-Bi_2O_3 (**a**), N-doped α-Bi_2O_3 (**b**), enlarged detail of N-doped α-Bi_2O_3 (**c**), pure β-Bi_2O_3 (d), N-doped β-Bi_2O_3 (**e**), and enlarged detail of N-doped β-Bi_2O_3 (**f**)

band gap renders β-Bi_2O_3 a more promising candidate for visible light driven photocatalytic applications. The band gap type of α-Bi_2O_3 and β-Bi_2O_3 does not change with N doping, whereas both Fermi levels shift downward to the VB, in line with the presence of a p-type dopant. For N-doped α-Bi_2O_3, the CBM shifts downward slightly compared with the pristine oxide, leading to a band gap narrowing by 0.17 eV, which is in agreement with the simulated band structures of N-doped α-Bi_2O_3 [12]. In contrast, the CBM for N-doped β-Bi_2O_3 remains almost unchanged after doping, i.e., N doping is not expected to result in an obvious band gap narrowing and the according red shift of the absorption spectrum. (ii) DOS plots show that for both α-Bi_2O_3 and β-Bi_2O_3, the top of valence bands (VBM) is mainly composed of Bi 6s and O 2p orbitals, whereas Bi 6p orbital contribute mainly to the bottom of both conduction bands (CBM). After substituting O with N, a narrow isolated band of gap state (IB) appears above the Fermi level at the top of VB, due to the N 2p orbital states. Since each N dopant has one less valence electron compared to O atom, the N-induced gap state acts as an acceptor level and results in p-type doping for both α-Bi_2O_3 and β-Bi_2O_3. Another evident effect is a certain VB band width broadening for N-doped α-

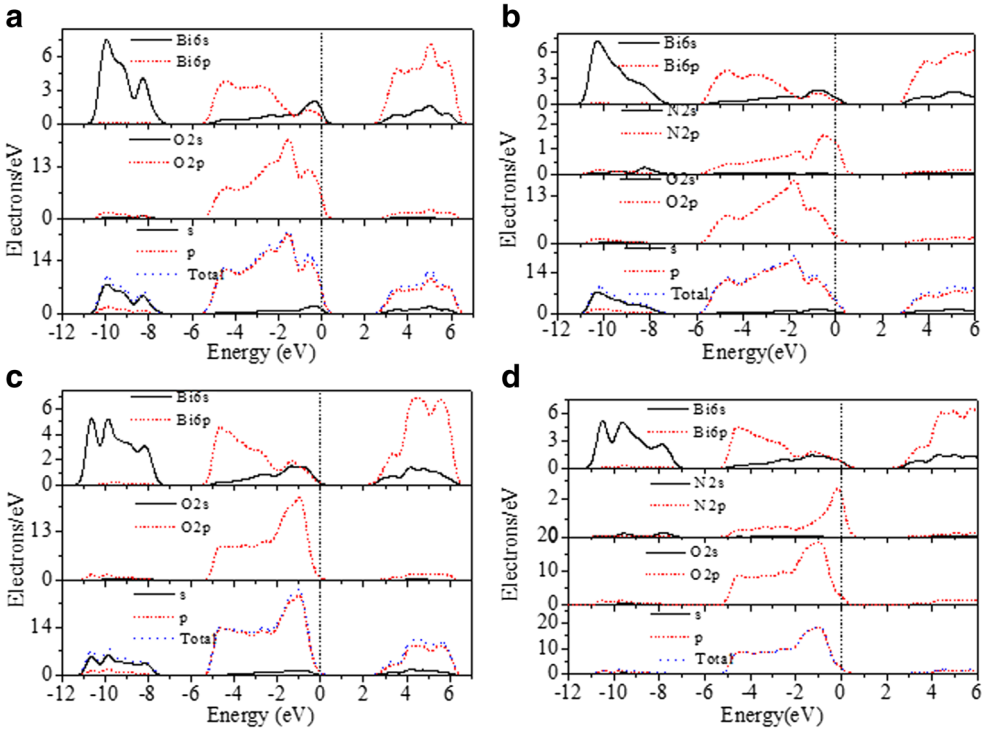

Fig. 4 Total and partial DOS of α-Bi_2O_3 (**a**), N-doped α-Bi_2O_3 (**b**), β-Bi_2O_3 (**c**), and N-doped β-Bi_2O_3 (**d**)

Bi_2O_3 and β-Bi_2O_3 along with a stronger fluctuation of the VB curves due to the hybridization of the N 2p states with Bi 6p and O 2p states, which leads to enhanced mobility of the photogenerated carriers.

The enlarged band structure near the Fermi level after N doping provides further insight into the electronic transitions (Fig. 3). The presence of new IBs leads to a two step optical transition from VB to CB, i.e., electrons move from the VB via the IB to the CB. Transition energies for the VB-IB step are 0.15 and 0.26 eV and for the second IB-CB step are 2.37 and 2.23 eV for N-doped α-Bi_2O_3 and β-Bi_2O_3, respectively, i.e., they are much smaller than the corresponding entire band gaps of N-doped and pure Bi_2O_3 forms. This facilitates electronic transitions under irradiation considerably and thus promotes electron–hole separation to enhance the photocatalytic performance in the visible light region. This is supported by the decreased fluorescence intensity in the fluorescence emission spectrum for N-doped Bi_2O_3 [11]. The smaller the fluorescence intensity, the lower the extent of recombination of photogenerated electron–hole pairs. Related IB band phenomena are also found in TiO_2 systems, such as C or N mono-doped rutile TiO_2 [25] and Bi/N co-doped anatase TiO_2 [28]. Calculation of the optical properties further confirms the results from band structure analysis (cf. next section).

Optical properties

Electron-photon interactions can result in transitions between the VB and the CB. The optical constants of a semiconductor can be deduced from the real part $\varepsilon_1(\omega)$ and imaginary part $\varepsilon_2(\omega)$ of the dielectric function. The absorption coefficient $\alpha(\omega)$ and the electron energy-loss function $L(\omega)$ can be obtained by using the following equations:

$$\alpha(\omega) = \sqrt{2}\omega\left(\sqrt{\varepsilon_1{}^2(\omega) + \varepsilon_2{}^2(\omega)} - \varepsilon_1(\omega)\right)^{1/2} \quad (2)$$

$$L(\omega) = \frac{\varepsilon_2(\omega)}{\varepsilon_1{}^2(\omega) + \varepsilon_2{}^2(\omega)} \quad (3)$$

The calculated absorption coefficient as a function of wavelength is presented in Figs. 5a and b for α-Bi_2O_3 and β-Bi_2O_3. Their absorption tailing stops at 550 and 650 nm, respectively, in line with the smaller band gap of β-Bi_2O_3. We note that the N-doping extends both absorption regions to longer wavelengths above 800 nm, with significant red-shifts of 250 and 150 nm for α-Bi_2O_3 and β-Bi_2O_3, leading to optical absorption in the overall visible light region as seen in UV–vis spectrum of N-doped Bi_2O_3 [11]. This effect stands in contrast to N-doped anatase TiO_2 which exhibits only minor variations of the absorption edge compared with pure TiO_2 [30]. Additional insights into the inter-band optical transitions can be gained by plotting $\varepsilon_2(\omega)$ as a function of energy (Figs. 5c and d), which can be obtained from the momentum matrix elements between the occupied and unoccupied wave functions within the selection rules. In the case of pure Bi_2O_3, the $\varepsilon_2(\omega)$ curves have smaller thresholds of transition compared with their band gaps, with major peaks at 5.2 and

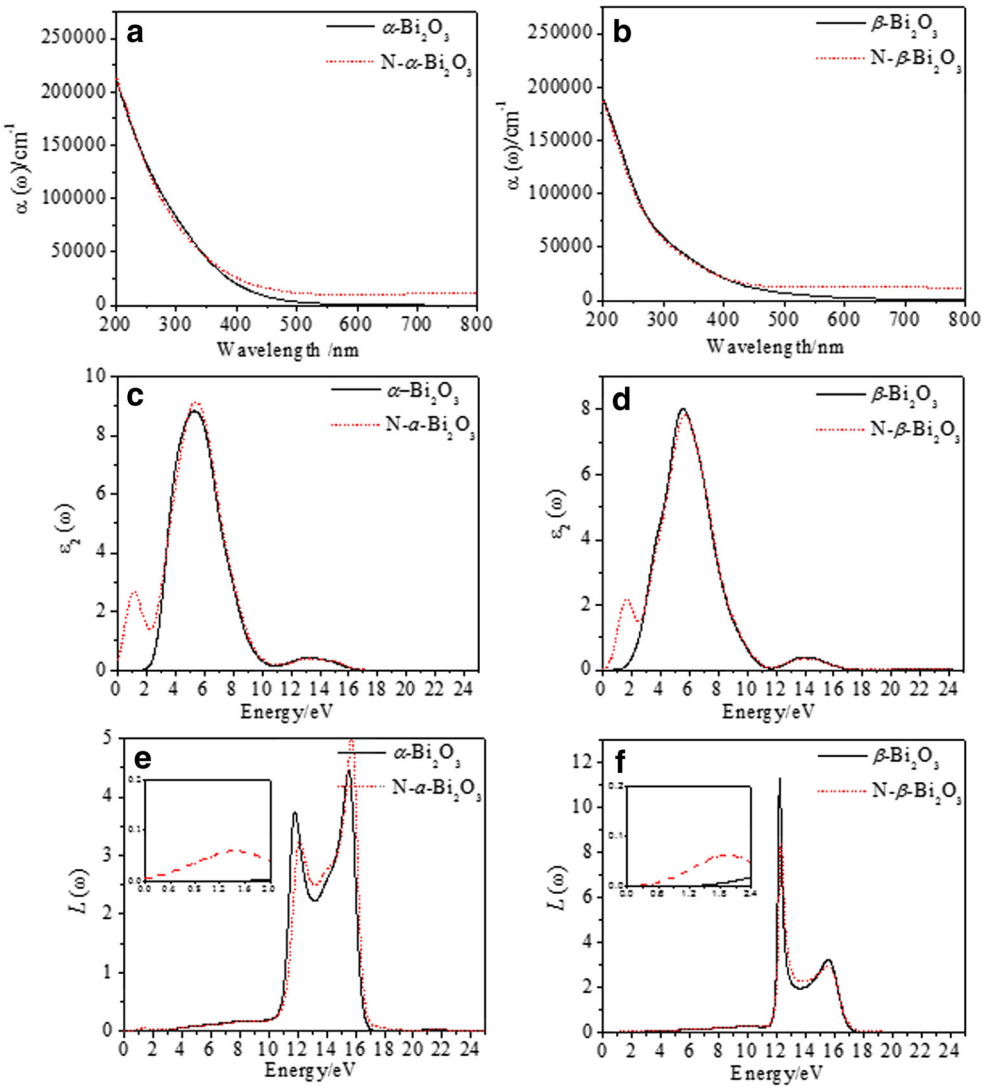

Fig. 5 Absorption spectra (**a**) and (**b**), imaginary part of dielectric functions (**c**) and (**d**), and electron energy-loss functions (**e**) and (**f**) for the pure and N-doped α-Bi_2O_3 and β-Bi_2O_3, respectively

5.6 eV for α-Bi_2O_3 and β-Bi_2O_3. These peaks mainly arise from electronic transitions from the O 2p levels in the VB to Bi 6p states in the CB. Beyond these main peaks, other minor peaks are located at 13.2 and 14.1 eV for α-Bi_2O_3 and β-Bi_2O_3, which originate from transitions from Bi 6s to Bi 6p levels. Whereas the positions of major and minor peaks in the high energy region remain virtually unchanged after N doping, a broad peak is observed for both N-doped α-Bi_2O_3 and β-Bi_2O_3 in the low energy region between 0 and 2 eV. Photons with according energy are sufficient to excite electrons from the O 2p level of the VB to the N 2p orbitals constituting the IB, which shows that the presence of IB acts as a step that facilitates electronic transitions under irradiation. The calculated optical properties thus confirm the above analysis of IB band structures. All in all, substitution of O by N in Bi_2O_3 induces significant red-shifts due to the presence of the IB levels which give rise to more convenient two step electronic transitions between VB and CB and leads to the improvement of visible-light driven photocatalytic activity observed in experiments [11, 12].

The electron energy-loss function $L(\omega)$ is plotted in Figs. 5e and f for both pristine and N-doped Bi_2O_3 forms as an important factor for quantifying the energy loss of a fast electron traversing a material. The peaks in the $L(\omega)$ vs. E plot represent plasma resonance, and the corresponding frequency is the so-called plasma frequency. The $L(\omega)$ spectra of α-Bi_2O_3 and β-Bi_2O_3 differ considerably due to the different crystal structures, with the former having two comparably broad peaks, and the latter with one sharp peak and another weak and broadened peak. First and second plasma peaks for both forms appear around 12 eV and 15 eV, respectively. These peaks arise from the electron transitions between Bi 6s in the deeper valence bands to Bi 6p states. As for N-doped crystals, the spectra shapes are quite similar to the pristine structures, which is consistent with the results of the structural analysis showing that N doping does not induce significant structural distortions.

Additionally, a broad and small peak appears in the low energy region (0–2 eV), which is attributed to the N-dopant induced electron transition from VB to IB.

Conclusions

We have carried out first principle studies on the crystal structure, electronic, and optical properties of N-doped Bi_2O_3 polymorphs. Whereas the lattice parameters and local structural environments are not substantially changed by N/O substitution, the charge density distribution is changed through apparent charge transfer from Bi to N. N-doped β-Bi_2O_3 exhibits higher thermodynamic stability than N-doped α-Bi_2O_3 according to band population analyses and lower defect formation energy. Interestingly, N doping does not lead to significant band gap narrowing but induces isolated bands composed of N 2p orbitals which lead to a two step electron transition between VB and CB. This facilitates electronic transition under irradiation and plays an important role in the significant calculated red-shift of the absorption spectra of both N-doped modifications and the enhanced photocatalytic performance in the visible light region observed in preceding experimental studies. The present study promotes the understanding of the promising photocatalytic properties of N-doped Bi_2O_3 and paves the way to tailoring this robust and low-cost material for technological applications. For visible-light activated photocatalysts, Bi_2O_3 systems have higher potential in the applications of electro-optic materials compared to TiO_2 which still attracts a lot of current attention. Concerning phase transformations of Bi_2O_3 polymorphs, the underlying mechanisms remain rather controversial and unclear. This calls for follow-up studies on the phase transition processes of N-doped Bi_2O_3 polymorphs.

Acknowledgments We thank the financial support by the National Natural Science Foundation of China (51102245), Sichuan Youth Science and Technology Foundation (2013JQ0034), the Innovative Research Team of Sichuan Provincial Education Department (2012XJZT002), Scientific Research Staring Project of SWPU (2014QHZ020, 2014PYZ012), and Sichuan Provincial Colleges' Sate Key Laboratory of Oil and Gas Reservoir Project (x151514kcl17)

References

1. Chen XB, Mao SS (2007) Chem Rev 107:2891–2959
2. Linsebigler AL, Lu G, Yates JT Jr (1995) Chem Rev 95:735–758
3. Wang F, Cao K, Zhang Q, Gong XD, Zhou Y (2014) J Mol Model 20:2506
4. Leontie L, Caraman M, Delibas M, Rusu GI (2001) Mater Res Bull 36:1629–1637
5. Muruganandham M, Amutha R, Lee GJ, Hsieh SH, Wu JJ, Sillanpää MJ (2012) Phys Chem C 116:12906–12915
6. Huang Q, Zhang S, Cai C, Zhou B (2011) Mater Lett 65988–65990
7. Cheng H, Huang B, Lu J, Wang Z, Xu B, Qin X, Zhang X, Dai Y (2010) Phys Chem Chem Phys 12:15468–15475
8. Romanov AN, Fattakhova ZT, Rufov YN, Shashkin DP (2001) Kinet Catal 42:275–280
9. Xia N, Yuan D, Zhou T, Chen J, Mo S, Liu Y (2011) Mater Res Bull 46:687–691
10. Dai G, Liu S, Liang Y (2014) J Alloys Compd 608:44–48
11. Lu YG, Yang YC, Xiang YZ, Liu SY (2012) J Inorg Mater 27:643–648
12. Jun S, Yuan G, Hao WC, Jing X, Ju HX, Wang L, Feng HF, Wang TM (2014) Chin Phys B 23:038103
13. Li M, Li F, Yin PG (2014) Chem Phys Lett 601:92–97
14. Asahi R, Morikawa T, Ohwaki T, Aoki K, Taga Y (2001) Science 293:269–271
15. Batzill M, Morales EH, Diebold U (2006) Phys Rev Lett 96:026103
16. Valentin CD, Pacchioni G, Selloni A (2004) Phys Rev B 70085116
17. Serpone N (2006) J Phys Chem B 110:24287–24293
18. Perdew JP, Wang Y (1992) Phys Rev B 45:13244
19. Vanderbilt D (1990) Phys Rev B 41:7892
20. Segall MD, Lindan PJD, Probert MJ, Pickard CJ, Hasnip PJ, Clark SJ, Payne MC (2002) J Phys: Condensed Mat 14:2717
21. Fischer TH, Almlof J (1992) J Phys Chem 96:9768–9774
22. Dong H, Chen G, Sun JX, Li CM, Yu YG, Chen DH (2013) Appl Catal B: Environmental 134:46–54
23. Lai KR, Zhu YT, Lu JB, Dai Y, Huang BB (2013) Comp Mater Sci 67:88–92
24. Wang J, Tafen DN, Lewis JP, Hong ZL, Manivannan A, Zhi MJ, Li M, Wu NQ (2009) J Am Chem Soc 131:12290–12297
25. Han XP, Shao GS (2011) J Phys Chem C 115:8274–8282
26. Yu JG, Zhou P, Li Q (2013) Phys Chem Chem Phys 151:2040–12047
27. Harwig HA (1978) Allg Chem 444:167–177
28. Wu GH, Zheng SK, Wu PF, Su J, Liu L (2013) Solid State Commun 163:7–10
29. Yang KS, Dai Y, Huang BB (2007) J Phys Chem C 111:12086–12090
30. Dashora A, Patel N, Kothari DC, Ahuja BL, Miotello A (2014) Sol Energ Mat Sol C 125:120–126